ChemComm
Chemical Communications

Accepted Manuscript

This article can be cited before page numbers have been issued, to do this please use: Z. Li, Y. Qi, L. Han, C. Zhang, Z. Yang, Z. Wu and S. Xu, *Chem. Commun.*, 2026, DOI: 10.1039/D5CC07291C.

ROYAL SOCIETY OF CHEMISTRY

rsc.li/chemcomm

View Article Online
DOI: 10.1039/D5CC07291C

COMMUNICATION

Dual-Temperature Photothermal Tandem Catalysis for CO_2 Conversion to Olefins

Ziyang Li[a], Yuhang Qi[a*], Lipu Han[a], Chu Zhang[a], Zhenwen Yang[a], Zhike Wu[a], Shanshan Xu[b,c*]

Received 00th January 20xx,
Accepted 00th January 20xx

DOI: 10.1039/x0xx00000x

We report a dual-temperature photothermal tandem system that overcomes this temperature mismatch and enables efficient CO_2 hydrogenation to light olefins in a single reactor. A graphene-modified In_2O_3 top bed drives the RWGS reaction and provides strong broadband absorption for efficient photothermal heating, thereby achieving higher temperatures for CO generation. The CO then feeds into a downstream K-doped Fe_2O_3 bed maintained at a lower temperature suitable for FTS to produce light olefins. This vertically arranged, dual-temperature configuration spatially separates and couples RWGS and FTS, effectively synchronising the tandem pathway. As a result, the system achieves a light-olefin production rate of 52.1 μmol g^{-1} h^{-1} with 69% selectivity at 0.05 MPa under photothermal conditions without external heating.

The increasing atmospheric CO_2 level is aggravating climate change and energy insecurity, highlighting the urgent need for sustainable carbon-recycling technologies.[1, 2] Among the various strategies, photothermal CO_2 reduction has attracted growing attention because it does not require external electrical input and enables full-spectrum solar utilization to activate inert CO_2 molecules. [3, 4] Significant progress has been achieved in CO_2 hydrogenation to C_1 products such as CH_4, CO, and CH_3OH.[5, 6] However, overcoming the kinetic barriers associated with C–C bond formation to directly produce C_{2+} hydrocarbons remains highly challenging.[7, 8]

For thermocatalytic CO_2 hydrogenation towards C_{2+} products, two tandem strategies are most frequently explored. One approach involves coupling CO_2-to-methanol with a subsequent methanol-to-olefins (MTO) process. [9, 10] Although this route can yield light olefins, methanol selectivity is highly pressure-dependent. It typically requires elevated pressures to suppress methanol decomposition, which is unfavourable for scalable operations under photothermal conditions. Another widely studied route converts CO_2 to CO via the reverse water–gas shift (RWGS) reaction, followed by Fischer–Tropsch synthesis (FTS) to form hydrocarbons. [11-13] Integrating RWGS and FTS in a single reactor is intrinsically difficult because the two steps requires different optimal temperature windows: RWGS is endothermic and favours high temperatures at > 400 °C for efficient CO formation,[14, 15] whereas FTS requires moderate temperatures (200–350 °C) to promote C–C coupling and avoid excessive methane formation.[16, 17] This fundamental temperature mismatch is a key limitation to achieving direct CO_2-to-olefins conversion in a single photothermal reactor.

Compared with the recently reported single-reactor tandem photothermal system, [18] this work employs a dual-bed reactor in which the RWGS and FTS functions are spatially separated. This design enables cascade heat utilization, suppresses local overheating, and allows independent optimization of each catalytic bed for improved flexibility in tuning target products. The top layer, made of graphene-modified In_2O_3 (G-In_2O_3), exhibits excellent photothermal conversion and efficiently reduces CO_2 to CO while simultaneously heating the gas phase and transferring heat to the downstream bed via combined radiative and convective heat transfer. This controlled heat flow determines the lower temperature of the potassium-doped Fe_2O_3 (K-Fe_2O_3) bed, where CO undergoes FTS to produce light olefins with high selectivity. The vertically stacked configuration establishes a well-defined temperature gradient, enabling the RWGS and FTS stages to operate within their respective optimal temperature ranges. Under low pressure (0.05 MPa), the tandem system achieves a light-olefin production rate of 52.1 μmol g^{-1} h^{-1} with 69% selectivity, demonstrating that engineering a temperature gradient is an effective strategy to overcome the inherent temperature mismatch in tandem photothermal catalysis.

The G-In_2O_3 composite in the top bed was prepared by using the hydrothermal method. The average particle size of In_2O_3 particles is 50–100 nm and is uniformly dispersed on the graphene sheets (Figure S1). The high-resolution transmission electron microscopy (HRTEM) image (Figure 1a) shows a distinct interface between graphene and In_2O_3. The corresponding fast Fourier transform patterns provide atomic-resolution structural

[a] School of Electronics and Infomation Engineering, Hebei University of Technology, Tianjin 300130, China
[b] *Department of Materials, School of Natural Science, The University of Manchester, Oxford Road, Manchester M13 9PL, UK*
[c] *University of Manchester at Harwell, Harwell Science and Innovation Campus, Didcot, Oxfordshire OX11 0DE, UK*
Supplementary Information available: See DOI: 10.1039/x0xx00000x

View Article Online
DOI: 10.1039/D5CC07206C

information: the cubic lattice spots can be assigned to In_2O_3, while the hexagonal pattern arises from the characteristic six-fold symmetry of graphene. Raman spectroscopy further confirms the formation of the G-In_2O_3 composite (Figure 1b). The D band at ~1300 cm^{-1} and G band at ~1400 cm^{-1} are characteristic of graphene, whereas the peaks at 307, 366, 494, and 628 cm^{-1} are aligned with the In–O vibrations of InO_6 structural units in the body-centred cubic In_2O_3 structure.

Potassium modification of Fe_2O_3 in the lower catalyst bed was verified by SEM and elemental mapping, which shows that K is homogeneously distributed on the Fe_2O_3 (Figure 1c). TEM and HRTEM analyses indicate that the lattice spacings of K-Fe_2O_3 are 0.251, 0.208, and 0.295 nm, corresponding to the (311), (400), and (220) crystal planes of γ-Fe_2O_3 (Figure S2). As shown in the X-ray diffraction (XRD) patterns (Figure 1d), all diffraction peaks can be indexed to Fe_2O_3 (JCPDS No. 39-1346) and In_2O_3 (JCPDS No. 71-2194),[19, 20] indicating that the crystalline structures of both oxides are preserved after graphene and K modification.

In the catalyst selection for this dual-bed reactor, In_2O_3 was chosen because it is an efficient catalyst for the RWGS reaction and can produce CO with nearly 100% selectivity. The generated CO acts as the substrate for the FTS reaction, thereby initiating the tandem reaction. Fe_2O_3 was selected instead of Fe_5C_2 because it offers advantages such as facile preparation, low cost, and good structural stability. In addition, Fe_2O_3 can be transformed into the active Fe_5C_2 phase through in situ phase conversion under reaction conditions.

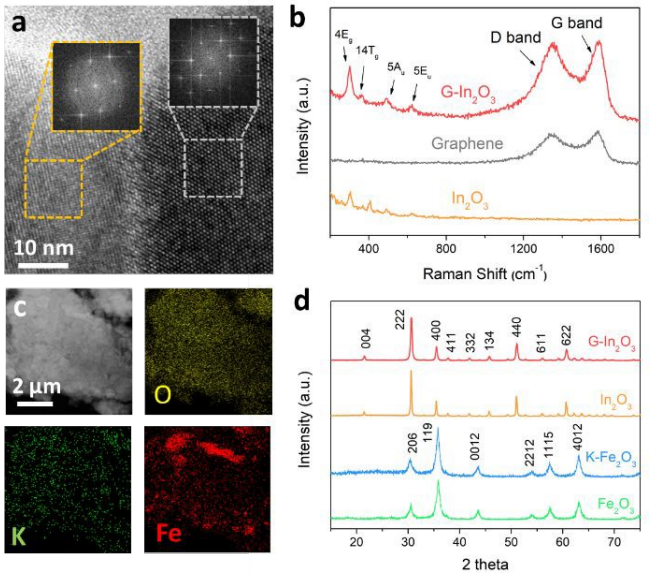

Figure 1. (a) The HRTEM image of G-In_2O_3-10% and corresponding Fast Fourier transform, (b) The Raman spectrum of graphene, In_2O_3 and G-In_2O_3-10%, (c) The element mapping of K-Fe_2O_3-5%, (d) The XRD pattern of In_2O_3, G-In_2O_3-10%, Fe_2O_3 and K-Fe_2O_3-5%.

To determine the optimal composition for CO_2 conversions, we evaluated G-In_2O_3 composites with various graphene loadings in the photothermal RWGS reaction (Figure S3) and K-modified Fe_2O_3 with different K contents in FTS (Figure S4). As shown in Figure S5, all the G-In_2O_3 composites produce CO as the only product, confirming that graphene incorporation does not alter the reaction pathway. The CO production rate increases progressively, reaching a maximum for G-In_2O_3-10%, but drops when the loading is further increased to 15 wt%. At moderate loadings (<10 wt%), graphene improves the dispersion of In_2O_3 and its specific surface area (Figure S6), and enhances CO_2 adsorption and activation (Figure S7).[21] The strong broadband absorption of graphene raises the catalyst surface temperature under illumination, thereby accelerating the endothermic RWGS reaction (Figure S8).[22] Graphene also suppresses non-radiative recombination of photogenerated carriers in In_2O_3, resulting in higher photothermal conversion efficiency (Figure S9).[23, 24] Such effects contribute to the enhanced CO production at the optimal 10 wt% loading. However, excessive graphene loadings will block In_2O_3 active sites and reduce accessible surface area for gas adsorption, leading to reduced CO production.

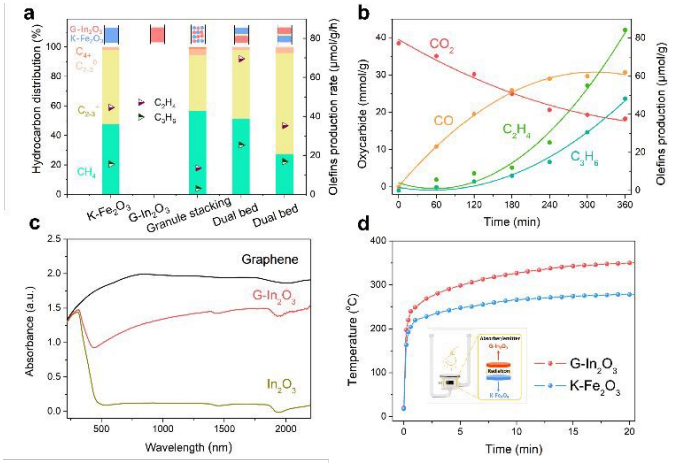

Figure 2. (a) Effect of the integration mode of G-In_2O_3-10% and K-Fe_2O_3-5% (mass ratio 3:5) on hydrocarbon distribution and light-olefin production rate under identical photothermal CO_2 hydrogenation conditions. (b)Time profiles of CO_2, CO, C_2H_4 and C_3H_6 over the dual-bed G-In_2O_3-10%/K-Fe_2O_3-5% catalyst under continuous illumination. (c) The UV-Vis-NIR spectrum of graphene, In_2O_3 and G-In_2O_3-10%, (d) Time evolution of the surface temperature of the G-In_2O_3-10% and K-Fe_2O_3-5% beds.

In the following FTS reaction, introducing potassium significantly changes both hydrocarbon distribution and light-olefin productivity. As shown in Figure S10, the K-Fe_2O_3 catalyst containing 2.5 wt% K exhibits the highest light-olefin production rate (i.e., 0.55 mmol/g/h for C_2H_4 and 0.37 mmol/g/h for C_3H_6). In contrast, although the overall olefin production rate declines at higher K loadings, the K-Fe_2O_3 with 5 wt% K catalyst shows the highest selectivity toward $C_{2\text{-}3}^{=}$ olefins (51%), accompanied by a suppressed formation of CH_4. A moderate amount of potassium improves the catalytic performance by slightly reducing the photoluminescence intensity of Fe_2O_3 (Figure S11), and enhancing CO adsorption and activation (Figure S12). The broad desorption peak around 450 °C corresponds to the recombinative desorption of dissociatively adsorbed CO. However, excessive K loading further neutralises surface acidity and suppresses H_2 chemisorption, thus lowering the FTS reaction rate and shifting the product distribution away from CH_4 and toward heavier hydrocarbons and a higher olefin fraction, which agrees with the trends in Figure S10. [25, 26] Furthermore, the photothermal FTS performance of K-Fe_2O_3

was evaluated under identical conditions while varying the light intensity, as detailed in Figure S13.

After optimising the compositions of G-In_2O_3 and K- Fe_2O_3, we evaluated tandem photothermal CO_2 hydrogenation over the G-In_2O_3-10% and K-Fe_2O_3-5% catalyst. The hydrocarbon selectivity and product distribution depend strongly on the integration configuration of the two components. The single K-Fe_2O_3 component shows low activity and poor olefin selectivity (i.e., 50%) because it cannot accumulate sufficiently high CO concentrations, allowing the Sabatier reaction to proceed and producing CH_4 (i.e., 48%) as the product (Figure 2a and S14). In contrast, single In_2O_3 primarily generates CO as a product with negligible hydrocarbons, as the low-pressure and high-temperature conditions are unfavourable for methanol or olefin formation. Simply physical mixing of two components (granule stacking) shows only a minor tandem effect, indicating that excessive proximity does not enable optimal photothermal CO_2-to-olefins performance.

Therefore, we adopt a dual-bed configuration, with G-In_2O_3-10% in the upper layer and K-Fe_2O_3-5% in the lower layer, separated by an inert screen (Figure 2a). When K-Fe_2O_3-5% is positioned beneath G-In_2O_3-10%, the light-olefin production rate achieved 52.1 μmol g^{-1} h^{-1} with a selectivity of 69%. In contrast, reversing the order—placing K-Fe_2O_3-5% above G-In_2O_3-10% —resulted in a significantly lower olefin productivity, confirming that efficient tandem CO_2 reduction and F–T coupling requires the correct thermal and reactant-flow sequence. This improvement arises from the temperature distribution and reaction dynamics revealed in Figure 2b. In the dual-bed configuration, the upper G-In_2O_3-10% layer, operating at a higher photothermal temperature, rapidly converts CO_2 to CO and steadily increases the CO concentration throughout the reaction (Figure 2b). As CO continues to accumulate, the concentration surpasses the threshold required to trigger chain-growth reactions in the downstream FTS bed. Olefin production begins to rise significantly after 120 min and continues to increase over time. Meanwhile, the CO formation rate gradually approaches a quasi-steady state, while CO_2 is continuously consumed. These results demonstrate that the upper G-In_2O_3 bed must supply CO with high selectivity and rate to initiate and sustain FTS in the lower K-Fe_2O_3 bed, thereby enabling efficient tandem photothermal CO_2-to-olefins conversion. Detailed analysis of the stability test is provided in Figure S15 of the Supporting Information.

As a result, the photothermal conversion efficiency of the upper G-In_2O_3 layer is crucial. The light source primarily irradiates the top bed containing G-In_2O_3. G-In_2O_3 was selected because the tandem process is initiated by light-driven RWGS, which produces CO as the key intermediate for the subsequent FTS reaction in the lower bed. Positioning In_2O_3 in the upper bed promotes the formation of a CO-rich stream under continuous unidirectional gas flow. Moreover, UV–Vis–NIR spectra (Figure 2c) show that pristine In_2O_3, as a wide-band-gap semiconductor (3.2 eV, Figure S16), shows weak absorption across visible and near-infrared regions. Graphene endows G-In_2O_3 with strong, nearly broadband light absorption, enabling efficient photothermal conversion. The heat generated in the upper bed can also be transferred to the downstream K-Fe_2O_3 bed through thermal radiation and gas-phase convection, helping to maintain the temperature required for the tandem reaction. The resulting thermal distribution in the dual-bed configuration is confirmed under photothermal operation (Figure 2d): the upper G-In_2O_3 layer rapidly reaches ~360 °C within 10 min, while the lower K-Fe_2O_3 layer stabilises at ~260 °C. The respective temperatures also precisely correspond to the optimal adsorption range (Figure S17).

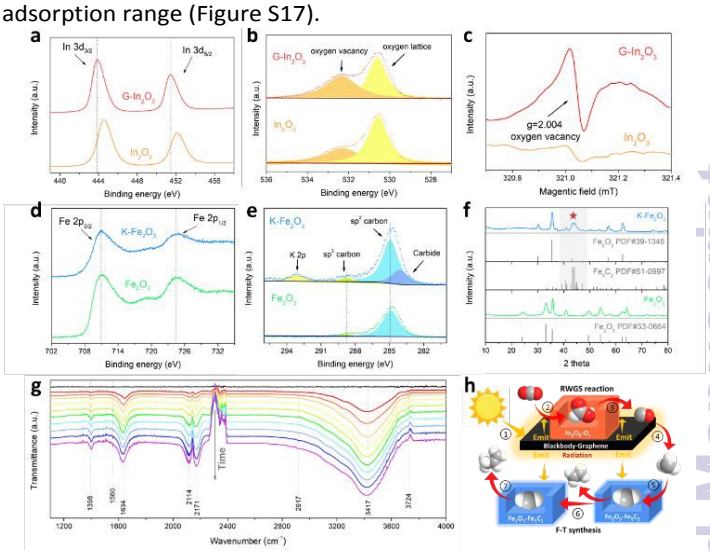

Figure 3. The XPS spectra of (a) In 3d and (b) O 1s, (c) The EPR of G-In_2O_3-10% and In_2O_3, The XPS spectra of (d) Fe 2p and (e) C 1s, (f) The XRD pattern of K-Fe_2O_3-5% and Fe_2O_3, (g) The in situ FTIR of G-In_2O_3-10% and K-Fe_2O_3-5%, (h) The advance and process of the photothermal CO_2 reduction to light olefin.

To identify the active sites in G-In_2O_3 for CO_2 reduction, XPS and EPR measurements were carried out. In comparison, the corresponding peaks of G-In_2O_3 shift to lower binding energies, which can be attributed to electron transfer at the graphene/In_2O_3 interface and an increased concentration of oxygen vacancies (Figure 3a). The O 1s spectra (Figure 3b) can be deconvoluted into two contributions: the peak at 529.8 eV is assigned to lattice oxygen in In–O–In, whereas the peak at 531.4 eV is associated with oxygen vacancies.[28] Furthermore, EPR spectra exhibit a signal at g = 2.004 (Figure 3c), which is characteristic of electrons trapped at oxygen vacancy sites.[29] The stronger EPR signal for G-In_2O_3 shows it has a higher oxygen-vacancy level, aligning with XPS results. This suggested that carbon at the graphene/In_2O_3 interface lowers the energy needed to create oxygen vacancies in the In_2O_3 lattice.

Because the oxygen vacancy concentration evolves under photothermal reaction conditions, we compared the XRD, PL, EPR and UV–vis–NIR spectra of G-In_2O_3 before and after the reaction (Figure S18-21). Detailed characterization and analysis are provided in the Supporting Information.

Regarding the active phase of K-Fe_2O_3 catalyst in the FTS reaction, XPS measurements were carried out to determine the surface elemental composition and chemical states (Figure 3d). In the Fe 2p spectrum, upon K promotion, the Fe $2p_{3/2}$ peak shifts to lower binding energy, indicating a more reduced Fe environment and thus facilitating the transformation of Fe species into Fe_5C_2, which is widely recognised as the active

phase for FTS in Fe-based catalysts.[30-32] In the C 1s spectrum (Figure 3e), three C 1s components together with an additional K 2p signal are observed. Compared with pristine Fe_2O_3, the K-Fe_2O_3 sample exhibits new carbide-related C 1s features, aligning with the leftward shift of the Fe $2p_{3/2}$ peak.[33] XRD patterns of Fe_2O_3 and K-Fe_2O_3 (Figure 3f) further reveal that additional reflections in K-Fe_2O_3 can be indexed to the main diffraction peaks of Fe_5C_2, with no Fe_3C phase detected (Detailed analysis is provided in Figure S22 of the Supporting Information.).[34, 35] K doping plays multiple roles in the Fe-based catalyst by enhancing CO adsorption and activation, increasing chain-growth probability, and suppressing the secondary hydrogenation of olefins, thereby improving light-olefin selectivity. In addition, K facilitates the formation and stabilization of the Fe_5C_2 active phase, which contributes to the enhanced FTS performance. [36]

Although In_2O_3 is widely recognized as an effective catalyst for CO_2 hydrogenation to methanol under relatively high pressures, the reaction in this work was performed at 0.5 atm, which is less favorable for methanol formation.[37] To elucidate the CO_2 activation pathway, in situ FTIR spectroscopy was conducted (Figure 3g). The spectra show a band at 1398 cm^{-1} assigned to carbonate species and a band at 1560 cm^{-1} attributed to $COOH^*$ intermediates. Since $COOH^*$ species are generally associated with the RWGS pathway to CO rather than the methanol pathway via $HCOO^*$, these results indicate that CO is the predominant product in the present system. The feature at 1634 cm^{-1} originates from adsorbed water, and the bands at 2114 and 2171 cm^{-1} are ascribed to linearly and bridge-bonded adsorbed CO*, respectively. The band at 2917 cm^{-1} is characteristic of CH_3^* species, and the broad absorptions at 3417 and 3724 cm^{-1} are associated with surface hydroxyl groups and adsorbed water molecules.[38] Accordingly, these surface intermediates provide direct spectroscopic evidence for a tandem RWGS–FTS mechanism, wherein CO_2 is first reduced to CO via RWGS, and then resulting CO is subsequently hydrogenated through CH_x^* intermediates to form light hydrocarbons.[39-41]

In summary, we have developed a tandem dual-temperature catalytic configuration that enables controlled multi-stage temperature distribution and efficient energy utilisation for the photothermal hydrogenation of CO_2 into high-value hydrocarbons. In the upper bed, G–In_2O_3 drives the RWGS reaction. The absorbed light energy is converted into heat and transmitted to the underlying K–Fe_2O_3 bed via both radiative and convective heat transfer. In the lower bed, K–Fe_2O_3 drives the FTS process (Figure 3h). By synergistically engineering the dual-bed catalysts with optimal operational temperatures in a single photothermal reactor, we achieve direct CO_2-to-light-olefin conversion with a production rate of 52.1 μmol g^{-1} h^{-1} and a selectivity of 69%, demonstrating a promising strategy for solar-driven CO_2 valorisation.

Author contributions

L.H., J.H., and Y.Q. Conceived and wrote this project. L.H. conducted a software simulation and collected and analysed experimental data. C.L. and Z.L. assisted with collecting experimental data and offered suggestions for revising the paper. S.X revised and concepted the manuscript.

Conflicts of interest

There are no conflicts to declare.

Data availability

The data supporting this article have been included as part of the SI. See DOI: https://doi.org/10.1039/d5cc04650e.

Acknowledgements

The authors would like to appreciate the support from the National Natural Science Foundation of China (52402246) and the Natural Science Foundation of Hebei (E2023202267). SX thanks the starting funding from the University of Manchester and the University of Manchester Harwell Campus.

Notes and references

1. F. Xu, F. Zhao, X. Deng, J. Zhang, J. Zhang, C. Ai, J. Yu and H. García, Nature Communications, 2025, 16.
2. X. Wan, Y. Li, Y. Chen, J. Ma, Y.-A. Liu, E.-D. Zhao, Y. Gu, Y. Zhao, Y. Cui, R. Li, D. Liu, R. Long, K. M. Liew and Y. Xiong, Nature Communications, 2024, 15.
3. Z. Xiao, L. Zhang, X. Tan, K. Sun, J. Li, L. Pan, J. J. Zou, G. Li and D. Wang, Advanced Functional Materials, 2025, 35.
4. X. Ding, W. Liu, J. Zhao, L. Wang and Z. Zou, Advanced Materials, 2024, 37.
5. W. Gao, Y. Li, D. Xiao and D. Ma, Journal of Energy Chemistry, 2023, 83, 62-78.
6. S. Khan, X. Dai, T. Ali, S. Mahmood, M. u. Haq, M. S. Riaz and Y. Hu, International Journal of Hydrogen Energy, 2023, 48, 24756-24787.
7. E. Ø. Pedersen, I.-H. Svenum and E. A. Blekkan, Journal of Catalysis, 2018, 361, 23-32.
8. Z. Li, L. Zhong, F. Yu, Y. An, Y. Dai, Y. Yang, T. Lin, S. Li, H. Wang, P. Gao, Y. Sun and M. He, ACS Catalysis, 2017, 7, 3622-3631.
9. S. Garg, Z. Xie and J. G. Chen, Nature Chemical Engineering, 2024, 1, 139-148.
10. L. Wang, Y. Sun, F. Zhang, J. Hu, W. Hu, S. Xie, Y. Wang, J. Feng, Y. Li, G. Wang, B. Zhang, H. Wang, Q. Zhang and Y. Wang, Advanced Materials, 2022, 35.
11. S. Ning, H. Ou, Y. Li, C. Lv, S. Wang, D. Wang and J. Ye, Angewandte Chemie International Edition, 2023, 62.
12. H. Song, K. Sun, H. Huang, S. Ning, S. Wang, Z. Wang, Y. Weng, Y. Cui, Y. Li, X.-s. Wang, D. Wang, L. Liu, Z.-j. Wang and J. Ye, Nature Communications, 2025, 16.
13. R. Li, Y. Li, Z. Li, S. Ouyang, H. Yuan and T. Zhang, Advanced Materials, 2023, 35.
14. S. Mo, S. Li, J. Zhou, X. Zhao, H. Zhao, X. Zhou, Y. Fan, Z. Zhu, B. Li, Q. Xie, W. Si, Y. Chen, D. Ye and J. Li, ACS Catalysis, 2025, 15, 2796-2808.
15. L. Wang, Y. Dong, T. Yan, Z. Hu, F. M. Ali, D. M. Meira, P. N. Duchesne, J. Y. Y. Loh, C. Qiu, E. E. Storey, Y. Xu, W. Sun, M. Ghoussoub, N. P. Kherani, A. S. Helmy and G. A. Ozin, Nature Communications, 2020, 11.
16. Z. Xie, X.-Y. Yu, Z. Zhang, X. Wang and T. Xie, ACS Applied Materials & Interfaces, 2025, 17, 19617-19628.
17. Q. Hao, Z. Li, Y. Shi, R. Li, Y. Li, S. Ouyang, H. Yuan and T. Zhang, Nano Energy, 2022, 102.

View Article Online
DOI: 10.1039/D5CC07291C

18. S. Ning, X. Wu, H. Song, X. Ma, S. Yue, S. Zhang, L. Tang, R. Liu, X. Yin, S. Ouyang and J. Ye, Journal of the American Chemical Society, 2025, 148, 1728-1740.
19. P. Cao, X. Xu, F. Jia, Y. Zeng, W. Liu, C. Wang, S. Han, M. Fang, X. Liu, D. Zhu and S. T. Navale, Applied Surface Science, 2025, 688.
20. C.-Q. Guo, H.-S. Zheng, J. Yang, X. Xiang and Z.-Y. Zhao, Applied Surface Science, 2025, 685.
21. F. Hu, X. Chen, Z. Tu, Z.-H. Lu, G. Feng and R. Zhang, Industrial & Engineering Chemistry Research, 2021, 60, 12235-12243.
22. Z. Zhang and Z. Zhu, Applied Surface Science, 2022, 601.
23. X. Jin, Q. Guan, T. Tian, H. Li, Y. Han, F. Hao, Y. Cui, W. Li, Y. Zhu and Y. Zhang, Applied Surface Science, 2020, 504.
24. M. A. M. Khan, R. Siwach, S. Kumar, J. Ahmed and M. Ahamed, Journal of Alloys and Compounds, 2020, 846.
25. J. Huang, G. Zhang, M. Wang, J. Zhu, F. Ding, C. Song and X. Guo, Frontiers in Energy Research, 2023, 10.
26. H. Zhang, H. Ma, H. Zhang, W. Ying and D. Fang, Catalysis Letters, 2011, 142, 131-137.
27. P. Bredy, D. Farrusseng, Y. Schuurman and F. C. Meunier, Journal of Catalysis, 2022, 411, 93-96.
28. C. Shen, K. Sun, R. Zou, Q. Wu, D. Mei and C.-j. Liu, Applied Catalysis B: Environment and Energy, 2025, 361.
29. X. Yu, Y. Chen, Q. Zhang, Y. Yin, D. Sun, Y. Ru and G. Tian, Surfaces and Interfaces, 2023, 38.
30. L. Song, S. Ouyang, P. Li and J. Ye, Journal of Materials Chemistry A, 2022, 10, 16243-16248.
31. Z. Zhang, B. Chen, L. Jia, W. Liu, X. Gao, J. Gao, B. Meng, Y. Tan, Y. He, W. Tu and Y.-F. Han, Applied Catalysis B: Environmental, 2023, 327.
32. H. Wang, X. Nie, Y. Liu, M. J. Janik, X. Han, Y. Deng, W. Hu, C. Song and X. Guo, ACS Applied Materials & Interfaces, 2022, 14, 37637-37651.
33. M. A. Hoque, M. I. Guzman, J. P. Selegue and M. K. Gnanamani, Materials, 2022, 15.
34. S. Najari, S. Saeidi, A. Sápi, Á. Szamosvölgyi, Á. Papp, A. Efremova, H. Bali and Z. Kónya, Chemical Engineering Journal, 2024, 485.
35. Y. Liu, Y. Ye, Y. Li, H. Du, Z. Yin, M. Li, Z. Huang, X. Zheng, H. Wang, Y. Wang and Y. Deng, Molecular Catalysis, 2024, 556.
36. L. Niu, X. Liu, X. Wen, Y. Yang, J. Xu and Y. Li, Catalysis Today, 2020, 343, 101-111.
37. J. Ye, C. Liu, D. Mei and Q. Ge, ACS Catalysis, 2013, 3, 1296-1306.
38. T. Yan, L. Wang, Y. Liang, M. Makaremi, T. E. Wood, Y. Dai, B. Huang, F. M. Ali, Y. Dong and G. A. Ozin, Nature Communications, 2019, 10.
39. M. Zhang, J. Ren and Y. Yu, ACS Catalysis, 2019, 10, 689-701.
40. R. Li, Y. Li, Z. Li, W. Wei, Q. Hao, Y. Shi, S. Ouyang, H. Yuan and T. Zhang, ACS Catalysis, 2022, 12, 5316-5326.
41. J. Han, W. Liu, L. Zhang, H. Ren, C. Wu, J. Zhang, C. Gong, G. Yang, H. Yang, S. Zhang, H. Wang, T. Ji, J. Li and P. Gao, ACS Catalysis, 2025, 15, 3940-3954.

View Article Online
DOI: 10.1039/D5CC07291C

Data availability

The data supporting this article have been included as part of the SI. See DOI: https://doi.org/10.1039/d5cc04650e.